Seismicity Induced by Longwall Coal Mining at the Thoresby Colliery, Nottinghamshire, U.K.

James P. Verdon[1*], J-Michael Kendall[1], Antony Butcher[1], Richard Luckett[2], Brian J. Baptie[2],

1. School of Earth Sciences, University of Bristol, Wills Memorial Building, Queen's Road, Bristol, U.K., BS8 1RJ.

2. British Geological Survey, The Lyell Centre, Research Avenue South, Edinburgh, U.K., EH14 4AP.

* Corresponding Author. Email: James.Verdon@bristol.ac.uk, Tel: 0044 117 331 5135.

ABSTRACT

The U.K. has a long history of deep coal mining, and numerous cases of mining-induced seismicity have been recorded over the past 50 years. In this study we examine seismicity induced by longwall mining at one of the U.K.'s last deep coal mines, the Thoresby Colliery, Nottinghamshire. After public reports of felt seismicity in late 2013 a local seismic monitoring network was installed at this site, which provided monitoring from February to October 2014. This array recorded 305 seismic events, which form the basis of our analysis.

Event locations were found to closely track the position of the mining face within the Deep Soft Seam, with most events occurring up to 300 m ahead of the face position. This indicates that the seismicity is being directly induced by the mining, as opposed to being caused by activation of pre-existing tectonic features by stress transfer. However, we do not observe correlation between the rate of excavation and the rate of seismicity, and only a small portion of the overall deformation is being released as seismic energy.

Event magnitudes do not follow the expected Gutenberg-Richter distribution. Instead, the observed magnitude distributions can be reproduced if a Truncated Power Law distribution is used to simulate the rupture areas. The best-fit maximum rupture areas correspond to the distances between the Deep Soft Seam and the seams that over- and underlie it, which have both previously been excavated. Our inference is that the presence of a rubble-filled void (or goaf) where these seams have been removed is preventing the growth of larger rupture areas.

Source mechanism analysis reveals that most events consist of dip-slip motion along near-vertical planes that strike parallel to the orientation of the mining face. These mechanisms are consistent with the expected deformation that would occur as a longwall panel advances, with the under- and over-burdens moving upwards and downwards respectively to fill the void created by mining. This further reinforces our conclusion that the events are directly induced by the mining process. Similar mechanisms have been observed during longwall mining at other sites.

Keywords

Geomechanics; Earthquake Source Observations; Induced seismicity; seismic anisotropy

1. INTRODUCTION

Seismicity induced by coal mining has been a common occurrence in the United Kingdom (e.g., Redmayne, 1988). Indeed, Wilson et al. (2015) estimated that between 20 – 30% of all earthquakes recorded in the UK between 1970 – 2012 were induced by coal mining. From the late 1980s onwards the rate of coal production has declined significantly, as has the rate of associated earthquakes (Figure 1).

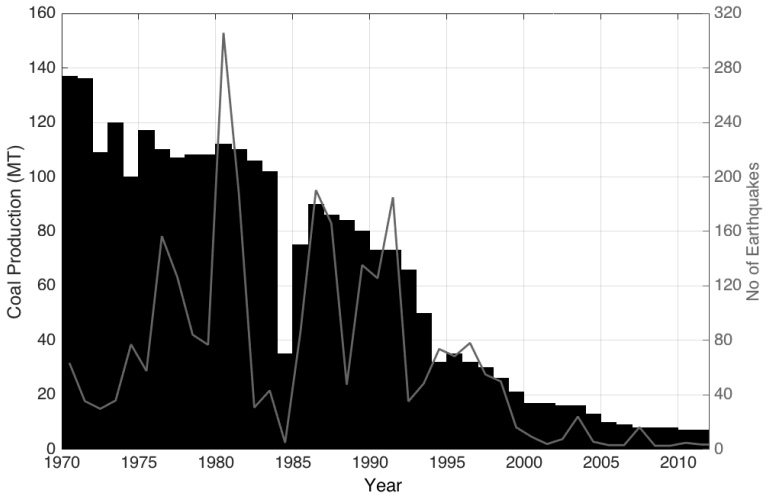

Figure 1: Deep mined coal production in the UK by year (bars) and the number of induced earthquakes per year associated with coal mining (grey line), as categorised by Wilson et al. (2015). The drop in both production and induced seismicity in 1984 is associated with the UK miner's strike.

Nevertheless, seismicity associated with deep coal mining still occurs in the UK. Between December 2013 – January 2014, the UK's national seismometer network detected a series of over 40 earthquakes near to the village of New Ollerton, Nottinghamshire. The largest of these events had a magnitude of $M_L = 1.7$. Given the generally low levels of seismicity in the UK, the village was dubbed the "UK's Earthquake Capital" (Turvill, 2014). The area has a history of seismic activity relating to coal mining (e.g., Bishop et al., 1993), and it was soon identified that the events were likely to be associated with longwall coal mining at the nearby Thoresby Colliery, which at the time was one of the few remaining deep coal mining sites in the UK.

In response to the felt earthquakes, a temporary local monitoring network of surface seismometers was deployed between the 5th February and the 30th October 2014 by the British Geological Survey (BGS). This network recorded a further 300 seismic events. The high quality of the data recorded by the local network permits a detailed study into the nature of seismicity and deformation induced by the longwall mining process.

1.1 Longwall Coal Mining at Thoresby

The Thoresby Colliery opened in 1925. Over the history of the site, at least 4 different seams have been mined, including the High Hazels, Top Hard, Deep Soft and Parkgate Seams, in order from shallowest to deepest: see Edwards (1967) for a stratigraphic section showing the positions of these and other seams in the region. The Deep Soft Seam was the last to be developed, with work beginning in 2010: this was the only seam being actively mined during the study period. The colliery closed entirely in mid-2015. This was for economic reasons, i.e. the low price of coal, not because of the induced seismicity.

The Deep Soft Seam was mined using standard longwall methods: hydraulic jacks are used to support the roof while a shearing device cuts coal from the face. As the face advances, the jacks are moved forward, allowing the roof to collapse into the cavity that is left behind. The collapsed, brecciated roof material filling this void is known as goaf (e.g. Younger, 2016). At Thoresby, each longwall panel has dimensions of approximately 300 m width, between 1,000 – 3,000 m length, and approximately 2.5 m height.

1.2 Seismicity Associated with Longwall Coal Mining

Seismicity has often been associated with the longwall mining process (e.g., Cook, 1976; Gibowicz et al., 1990; Bishop et al., 1993; Stec, 2007; Bischoff et al., 2010; Sen et al., 2013). Seismic events associated with coal mining have often been divided into two categories: "mining-tectonic" activity, produced by activation of pre-existing tectonic faults, and "mining-induced" activity, directly associated with the mining excavations (e.g., Stec, 2007).

Observed magnitudes have typically ranged from $0.5 < M_L < 3.5$. At some sites event magnitudes have followed the Gutenberg and Richter (1944) distribution (e.g., Bishop et al., 1993; Kwiatek et al., 2011), while in other cases bimodal or other frequency-magnitude distributions have been observed (e.g. Stec, 2007; Hudyma et al., 2008; Bischoff et al., 2010). These non-Gutenberg-Richter distributions have been attributed to the presence of characteristic length scales (the dimensions of the mined panels, for example) that provide a control on rupture dimensions and thereby event magnitudes.

Analysis of event focal spheres has revealed a variety of source mechanisms in different settings (e.g., Stec, 2007; Bischoff et al., 2010; Sen et al., 2013) including: non-double-couple events, indicating a volumetric component of deformation usually associated with the roof collapse process; double-couple events showing a direct relationship to mined panels, with vertical fault planes running parallel to the mining face, on which dip-slip motion occurs; and

107 double-couple events that correspond to regional fault orientations and *in situ* tectonic stress
108 conditions.

109 In this paper we follow the processes developed in the aforementioned studies to characterise
110 the seismicity induced by mining at the Thorseby Colliery. We begin by locating events,
111 comparing the event locations to the propagation of the mining faces with time, and
112 seismicity rates with the volume of coal extracted from the mine. We investigate the source
113 characteristics of the events, using spectral analysis combined with event frequency-
114 magnitude distributions to assess the length-scales of structures that have generated the
115 observed events. We use shear-wave splitting analysis to image *in situ* stress orientations at
116 the site, and we calculate focal mechanisms for the events to establish the orientations of fault
117 planes and slip directions generated by the mining process.

118

119 2. EVENT DETECTION AND LOCATION

120 *2.1. Monitoring array and event detection*

121 The local surface network deployed to monitor seismicity at the Thoresby Colliery comprised
122 of 4 3-component Guralp 3ESP broadband seismometers (stations NOLA, NOLD, NOLE and
123 NOLF) and 3 vertical-component Geotech Instruments S13J short-period seismometers
124 (NOLB, NOLC and NOLG)). The station positions are shown in Figure 2. Events were
125 detected using the BGS's in-house event detection algorithm, which is based on identification
126 of peaks in running short-time/long-time averages (STA/LTA), as described by Allen (1982).
127 A total of 305 events were identified during the deployment of the local monitoring network.

128 P- and S-wave arrival times were re-picked manually for every event (e.g. Figure 3). For most
129 event-station pairs the P-wave arrival was clear and unambiguous, and so could be accurately
130 picked (83% of station-event pairs where a pick could be manually assigned). Stations
131 NOLB, NOLC and NOLG were single, vertical component stations, so S-wave picks were not
132 made for these stations. For smaller events with lower signal-to-noise ratios, clear S-wave
133 arrivals were sometimes difficult to identify, resulting in a lower number of picks (74% of
134 station-event pairs where a pick could be manually assigned).

135 The velocity model used to locate the events is taken from Bishop et al. (1993), and is listed
136 in Table 1. The arrival time picks were inverted for the best-fitting location that minimises the
137 least-squares residual between modelled and picked arrival times. The search for the best-
138 fitting location was performed using the Neighbourhood Algorithm (Sambridge, 1999), and
139 the modelled travel times were calculated using an Eikonal solver (Podvin and Lecomte,

1991). A map of event hypocentres is shown in Figure 2, in which the mining panels and the position of the mining face with time are also shown.

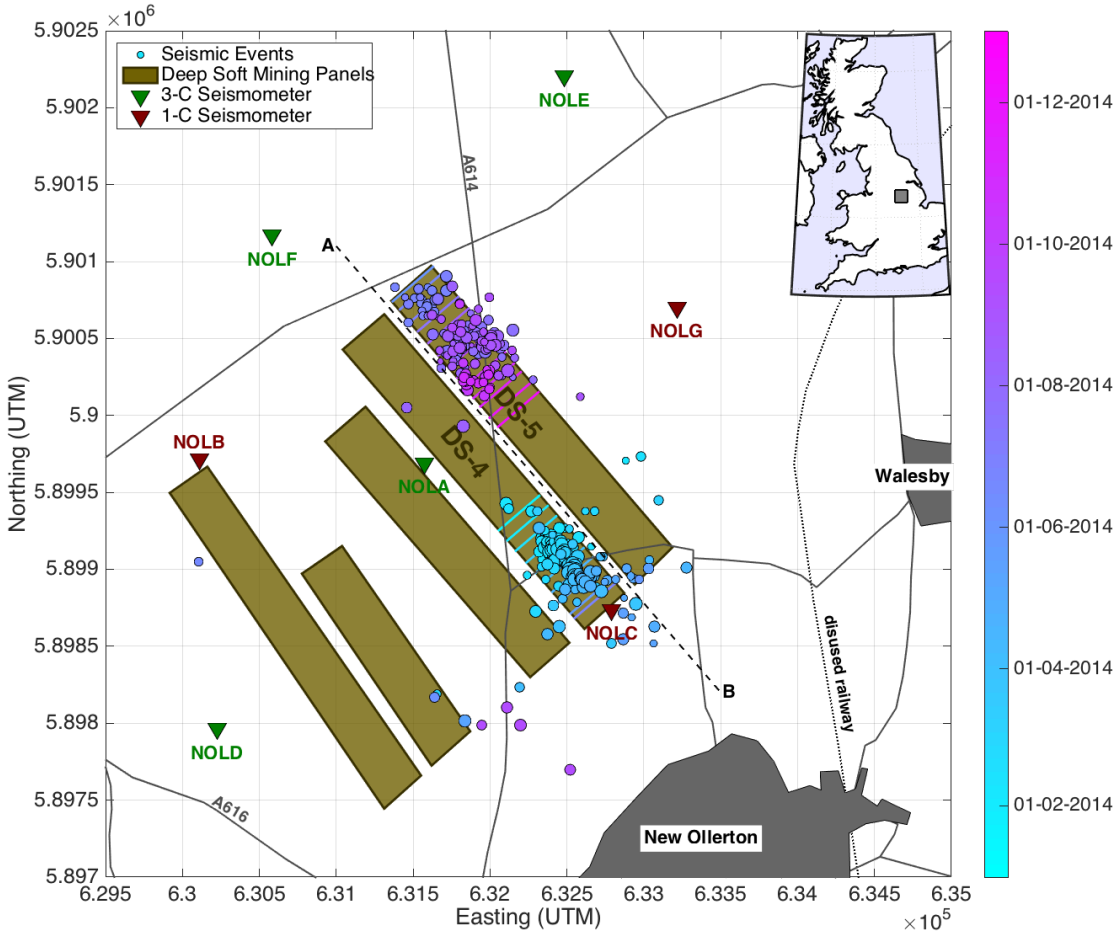

Figure 2: Map of event hypocentres, with events coloured by occurrence date. Also shown are the positions of the monitoring network (triangles) and the mining panels (brown rectangles). Panels DS-4 and DS-5 were active during the monitoring period, and the coloured bars running across these panels show the forward movement of the mining faces with time. The position of the cross-section A – B (Figure 5) is marked by the dashed line.

Layer No.	***Depth to Layer Top (m)***	***V_P (ms^{-1})***	***V_S (ms^{-1})***
1	0	1900	1280
2	60	2750	1540
3	135	3100	1740
4	275	3500	1970
5	1019	4200	2360
6	1351	5250	2920
7	2751	6000	3370

Table 1: 1D, layered, isotropic velocity model used to locate events. Model is based on that used by Bishop et al. (1993).

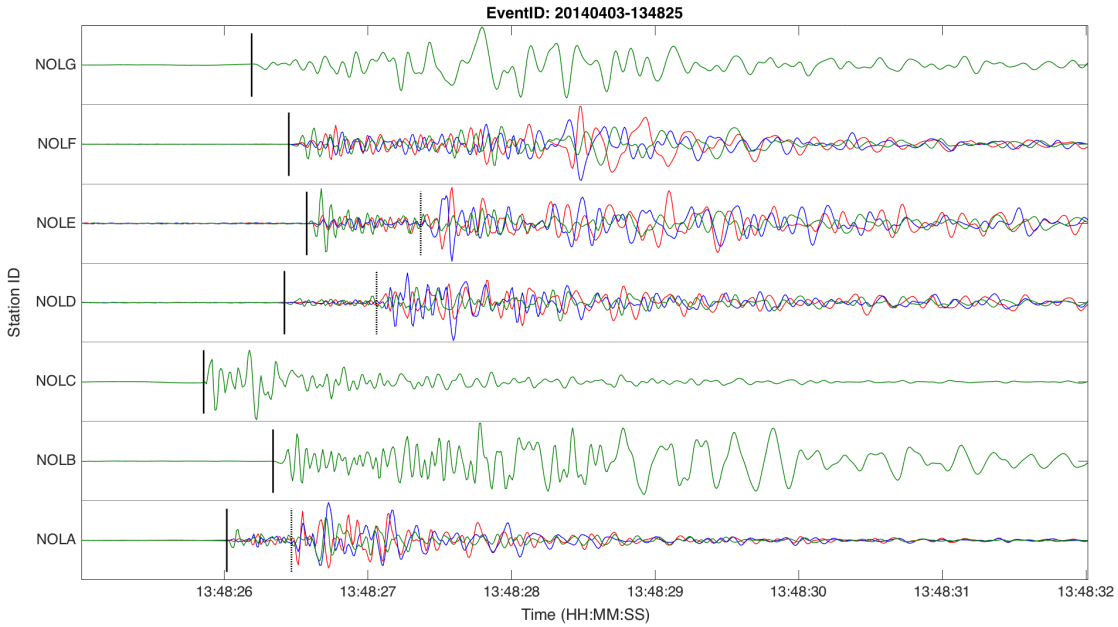

Figure 3: Recorded waveforms for a larger event (M_L = 1.3). The N (red), E (blue) and Z (green) components for each station are overlain. Stations NOLB, NOLC and NOLG are single (Z) component stations. The P- and S-wave picks are marked by the solid and dashed tick marks.

In Figure 4 we show histograms of the event location uncertainties laterally and in depth. Note that these uncertainties pertain solely to the residuals between picked and modelled arrival times, and do not account for velocity model uncertainties. The velocity model used is based on limited site-specific data, relying mainly on regional seismic refraction surveys (Bishop et al., 1993).

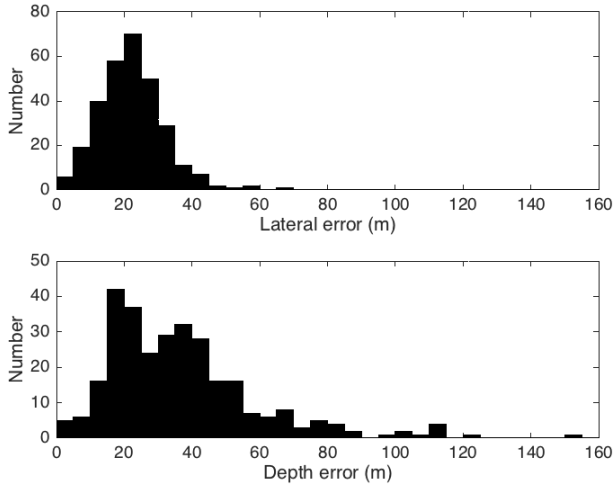

Figure 4: Histograms showing the lateral and depth uncertainties for the located events.

A brief sensitivity analysis suggested that velocity model uncertainties of up to 10% may affect depth locations by as much as 150m, while lateral locations are relatively unaffected. This reflects the geometry of the array, which provides reasonable azimuthal coverage but

with surface stations only, such that an uncertain velocity model will primarily affect the event depths.

Figure 5 shows a cross-section of event depths relative to the coal seams. We note that, while it appears that the events are located below the seam depths, given the likely velocity model uncertainties, it is not possible to rule out that these events are actually located at the same depths as the Deep Soft Seam being mined.

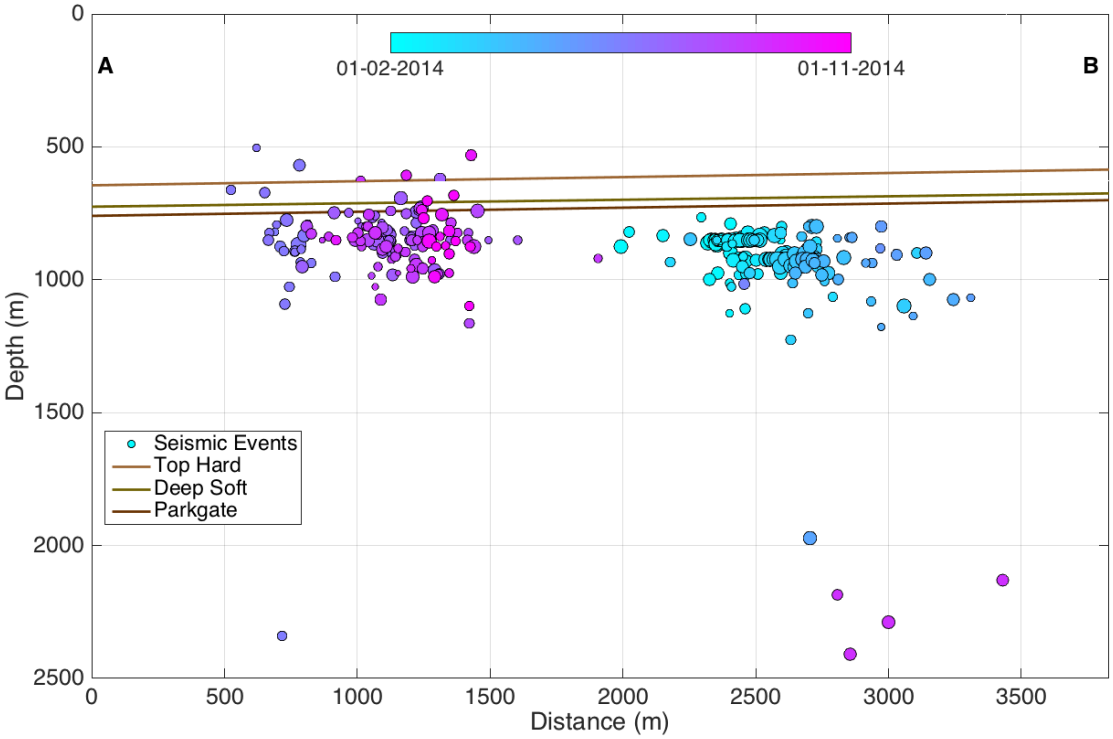

Figure 5: Events depths shown along cross-section A – B (see Figure 2). The positions of the Top Hard, Deep Soft and Parkgate Seams are also marked. Note that velocity uncertainties mean that the event depths may not be particularly well constrained.

2.2. Event Locations with Respect to Mining Activities

The positions of the mining panels, and the progress of the mining face with time, have been provided by the UK Coal Authority in their Mine Abandonment Plans (2017). The position of the mining face with respect to the events can be seen in Figure 2. It is immediately apparent that the event locations are tracking the position of the face as it moves SE along panel DS-4, before switching to DS-5 and again tracking the mining front to the SE. The monitoring period ceases when the events have propagated approximately half-way along the length of panel DS-5.

We investigate the position of events in relation to the mining face in greater detail in Figure 6, which shows a histogram of event positions relative to the mining face, along an axis parallel to the mining panels. Most events are found to occur ahead of the face, with most

events occurring within 300m of the face. This close correlation between events and the mining face implies that the events are being directly induced by mining activities, as opposed to the activation of pre-existing tectonic features, in which case we would expect the events to align along an activated fault. As per the categorisation described by Stec (2007), we characterise these as mining-induced events.

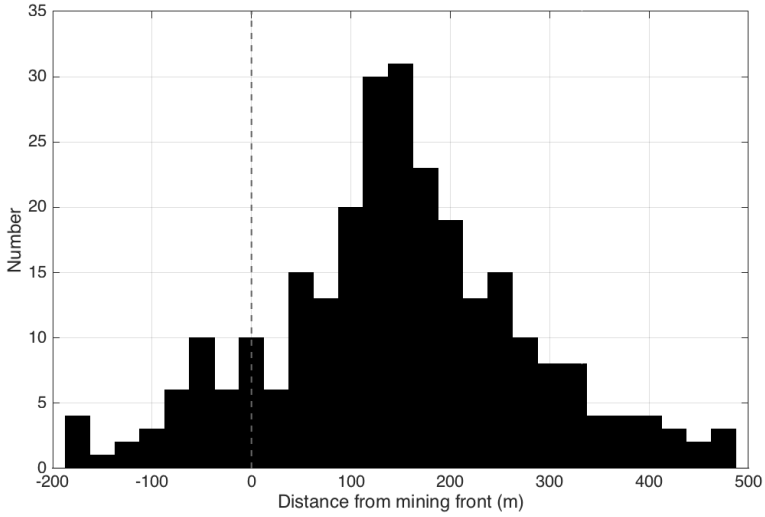

Figure 6: Histograms showing the lateral position of each event relative to the mining face at the time of event occurrence, where a positive distance represents events occurring in advance of the face.

However, we also note small cluster of 5 events that is found at greater depths (>2,000m), to the SW of the DS-4 panel. 4 of these 5 events occurred within a single 7-hour period. Establishing the causality of these events is more difficult. It is possible that these events have been have been triggered by the static transfer of stress changes to greater depths, leading to fault activation. As per the Stec (2007) categorisation, these may be mining-tectonic events. However, it is not possible to rule out that these deeper events may in fact have a natural origin.

3. Correlation Between Seismicity and Mining Rates?

In Figure 7 we show the volume of rock removed from the mine on a weekly basis (ΔV), the number of events per week (N_E), and the cumulative seismic moment (ΣM_O) released per week. The volume of rock removed per week is estimated from the forward progress of the mining face, multiplied by its dimensions (width and height). To further investigate any correlation between the extracted volume and seismicity, in Figure 8 we cross-plot these parameters. From Figure 8 it is apparent that there is little immediate correlation between ΔV and N_E and ΣM_O on a weekly basis.

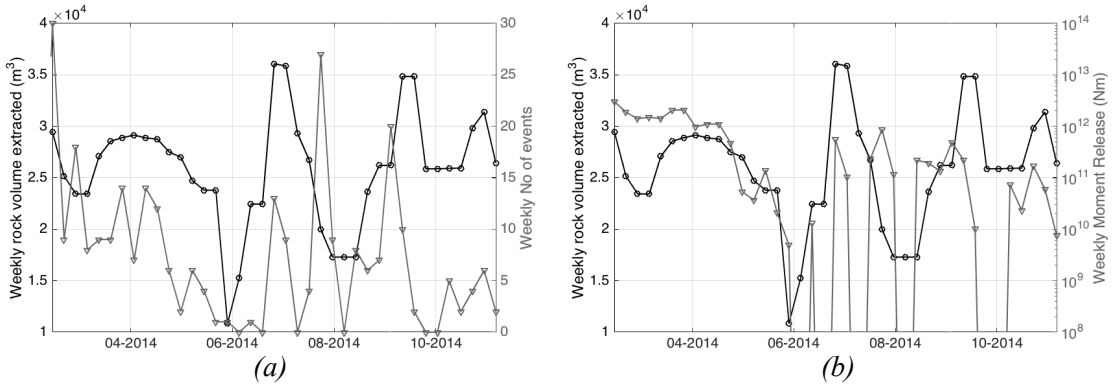

211 *Figure 7: Weekly rock volume extracted (black lines) compared with (a) the weekly number of*
212 *recorded events and (b) the weekly cumulative seismic moment released (grey lines).*

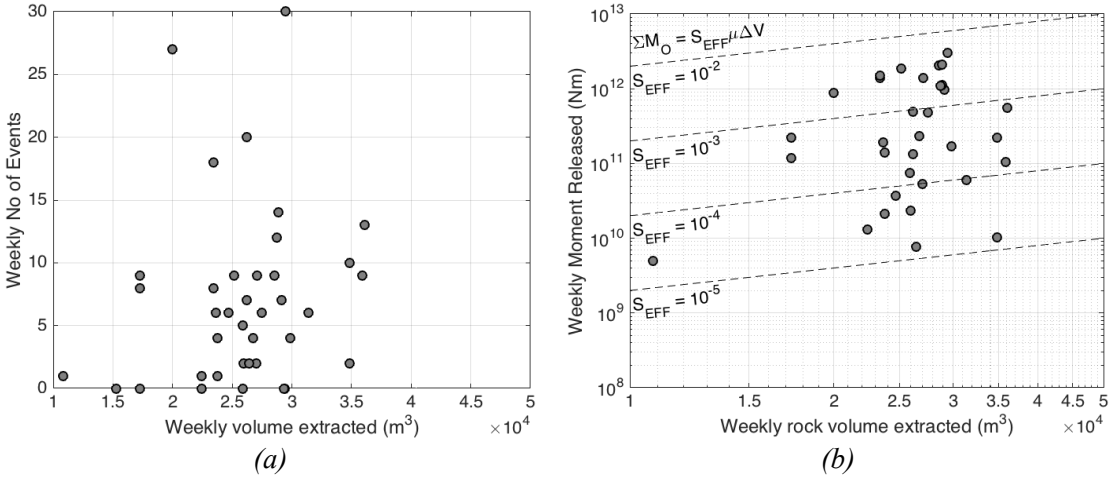

213 *Figure 8: Cross-plots examining potential correlation between weekly rock volume extracted and the*
214 *weekly number of recorded events (a) and the weekly cumulative seismic moment released (b). In (b),*
215 *the dashed lines show the expected relationship for given values of S_{EFF}.*

216 McGarr (1976) posited a linear relationship between ΔV and ΣM_O:

217 $$\Sigma M_O \approx \mu \Delta V, \quad (1)$$

218 where μ is the rock shear modulus. This relationship corresponds to the situation whereby all
219 of the deformation produced by the volume change is released seismically. In reality, much of
220 the deformation may occur aseismically. As such, Hallo et al. (2014) proposed a modification
221 to this relationship via a "seismic efficiency" term, S_{EFF}, which describes the portion of the
222 overall deformation that is released as seismic energy:

223 $$\Sigma M_O \approx S_{EFF} \mu \Delta V \quad (2)$$

224 In some of the most well-known cases of induced seismicity, values of S_{EFF} have been close
225 to 1 (e.g. McGarr, 2014). However, these cases represent outliers: during most industrial
226 operations S_{EFF} is much less that 1 (e.g., Hallo et al., 2014). The dashed lines in Figure 8(b)
227 show the relationship between ΔV, ΣM_O and S_{EFF}, assuming a generic value of μ = 20 GPa.
228 We note that the observed moment release rates correspond to values of S_{EFF} between 0.01 to

0.00001, implying that most of the deformation induced by the mining is released aseismically. This is typical for many cases of seismicity induced by a variety of industrial activities (e.g. Maxwell et al., 2008; Hallo et al., 2014)

4. Event Magnitudes and Frequency-Magnitude Distributions

4.1 Moment Magnitude Calculation

Local magnitudes for the Thoresby Colliery seismicity have been computed by Butcher et al. (2017), who found that the UK's existing local magnitude scale (Ottemöller and Sargeant, 2013) is not appropriate for use when sources and receivers are within a few kilometres of each other. This is because for nearby receivers, the raypath will be predominantly through the softer, more attenuative sedimentary cover, rather than the underlying crystalline crustal rocks, as will be the case for receivers that are more distant to the event. Butcher et al. (2017) have developed an alternative local magnitude scale based on the Thoresby events, which has been recalibrated to ensure consistency between magnitude measurements made on nearby stations and those made using the UK's permanent national monitoring network, the nearest stations of which were some distance from the Thoresby site.

However, our aim here is to investigate event magnitude distributions in order to understand the length scales of structures being affected by the mining process. This therefore requires the use of moment magnitudes, since seismic moment can be directly related to rupture dimensions. We compute moment magnitudes by fitting a Brune (1970) source model to the observed S-wave displacement amplitude spectra (Figure 9), following the method described by Stork et al. (2014). The seismic moment is determined from the amplitude of the low-frequency plateau, Ω_O.

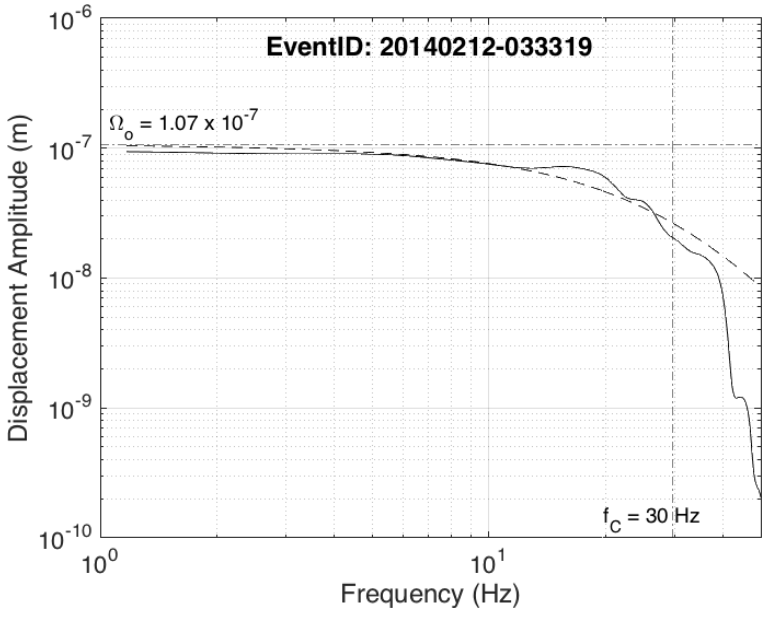

Figure 9: Example displacement spectrum used to estimate moment magnitudes. The solid line shows the observed spectrum, while the dashed line shows the best-fit Brune (1970) source model. The dot-dash lines show the f_C and Ω_O values for this model.

Ideally, the measured corner frequency, f_C, of the displacement spectra could be used to determine the rupture length. However, to robustly image the corner frequency, it must be significantly lower than the Nyquist frequency, f_N of the recording system – Stork et al. (2014) recommend that $f_N > 4f_C$ to obtain robust estimates of f_C. The recording systems at Thoresby had sampling rates of 100 Hz, so $f_N = 50$ Hz.

We can use generic values for stress drop and rupture lengths to establish the expected corner frequencies for events with $M_W < 1$. Using the relationships between rupture dimensions, seismic moment and stress drop given by Kanamori and Brodsky (2004), assuming a stress drop of 5 MPa and a rupture velocity of 2,000 m/s, the resulting corner frequency $f_C \approx 30$ Hz. Evidently, the $f_N > 4f_c$ criteria is not expected to hold for this particular dataset. However, our observations of event magnitudes, because they are derived from the amplitude spectra at low frequencies, are robust: we therefore use these to make inferences about the length scales of the structures that have generated the observed seismic events.

4.2. Frequency-Magnitude Distributions

The observed event magnitude distribution (EMD) is shown in Figure 10. We show the EMDs for the overall dataset, as well as individually for the clusters associated with the DS-4 and DS-5 panels. The overall dataset is not well described by the Gutenberg and Richter (1944) distribution $\log_{10} N(M) = a - bM$, where *N(M)* is the cumulative number of events larger than a given magnitude *M*, and *a* and *b* are constants to be determined. Such a distribution would be represented by a straight line in *M* vs $\log_{10}(N)$ space. We note that the apparent limit on the largest event size is not an artefact of a short measuring period: while the local array was removed in October 2014, the area continues to be monitored by the BGS National Seismometer Array, which has an estimated detection capability across the UK of magnitude > 2. Larger events occurring after the study period would therefore be detectable, but no such events have occurred.

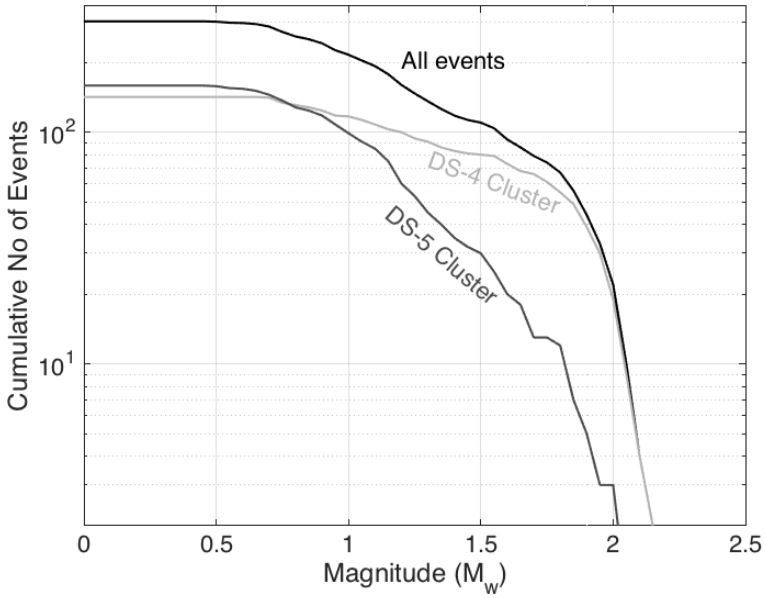

Figure 10: Observed frequency-magnitude distributions for the full event population (black), as well as for the DS-4 (light grey) and DS-5 (dark grey) clusters individually.

However, fault length and/or earthquake magnitude distributions that are constrained at some upper limit, leading to a fall-off from the power law relationship at large values, have been suggested by a number of authors. At the largest scale, Richter (1958) argues that "a physical upper limit to the largest possible magnitude must be set by the strength of crustal rocks, in terms of the maximum strain which they are competent to support without yielding". Similarly, Pacheco et al. (1992) argue that the rupture dimensions of very large earthquakes are limited by the thickness of the earth's seismogenic zone (the portion of the crust that is capable of undergoing brittle failure). For continental rift zones, Scholz and Contreras (1998) suggested that the maximum length of normal faults would be limited by the flexural restoring stress and friction, and found a good match between their model and faults in the East African Rift and in Nevada. At a much smaller scale, Shapiro et al. (2013) have suggested these effects will also apply to induced seismicity, with the maximum fault size, and therefore earthquake magnitude, determined by the dimensions of the volume stimulated by human activities.

To understand the observed EMDs at Thoresby, we consider the statistical distributions of fault rupture areas that might produce them. Typically, rupture areas are assumed to follow a self-similar, power law distribution (e.g., Wesnousky et al., 1983; Bonnet et al., 2001). If stress drops are assumed to be roughly constant (e.g. Abercrombie, 1995) then this power-law rupture area distribution will result in a power-law distribution of magnitudes, i.e. the Gutenberg-Richter distribution.

A cumulative power law (PL) distribution for rupture area will take the form:

$$N(L) = CA^{-\alpha}\,, \tag{3}$$

where $N(A)$ is the number of ruptures with area greater than length A, α is the power law exponent, and C is a constant. For a PL distribution, there is no upper limit to the maximum rupture area. Instead, if an upper limit to the rupture area is imposed, for example by the geometry of the mining panels, then a truncated power law (TPL) distribution results (Burroughs and Tebbens, 2001; 2002):

$$N(A) = C(A^{-\alpha} - {A_{MAX}}^{-\alpha}), \tag{4}$$

where A_{MAX} is the maximum rupture area.

To simulate event magnitudes based on rupture area, we use Kanamori and Brodsky (2004):

$$M_O = \Delta\sigma A^{3/2}, \tag{5}$$

where $\Delta\sigma$ is the stress drop. As discussed above, the limitation of a relatively low Nyquist frequency means that we cannot measure the stress drop directly. Therefore, to estimate the PL and TPL parameters that best-fit our observations, we initially assume a generic and arbitrary stress drop of $\Delta\sigma = 5$ MPa.

For each of the DS-4 and DS-5 event clusters, we perform a search over the PL and TPL parameters, finding those that minimise the least-squares misfit between observed and modelled EMDs. The resulting EMDs are shown as the solid lines in Figure 11, with the PL and TPL parameters, and the misfit for each of the models, listed in Table 2. The resulting rupture area distributions are shown in Figure 12.

Having established the best-fitting PL and TPL distributions with a fixed stress drop value, we then investigate the impact of a variable range of $\Delta\sigma$. We do this in a stochastic manner, simulating rupture area distributions based on the PL and TPL parameters, assigning stress drops randomly from a uniform distribution of $0.1 < \Delta\sigma < 20$ MPa. We repeat this process over 100 iterations, and in Figure 11 the dashed lines show the range encompassing ± 2 standard deviations around the resulting mean EMD. From Figure 11 we observe that both event populations are clearly better modelled by a TPL rupture area distribution, even when stochastic variation in $\Delta\sigma$ is considered.

	Dist. Type	***α***	***C***	***A_{MAX}***	***Misfit***
DS-4	PL	0.47	1707	NA	5.46
	TPL	0.1	743	10075	1.23
DS-5	PL	0.74	6861	NA	3.05
	TPL	0.38	1536	3870	0.86

Table 2: Best fitting power law and truncated power law distributions for each of the DS-4 and DS-5 clusters, and the resulting normalised misfits.

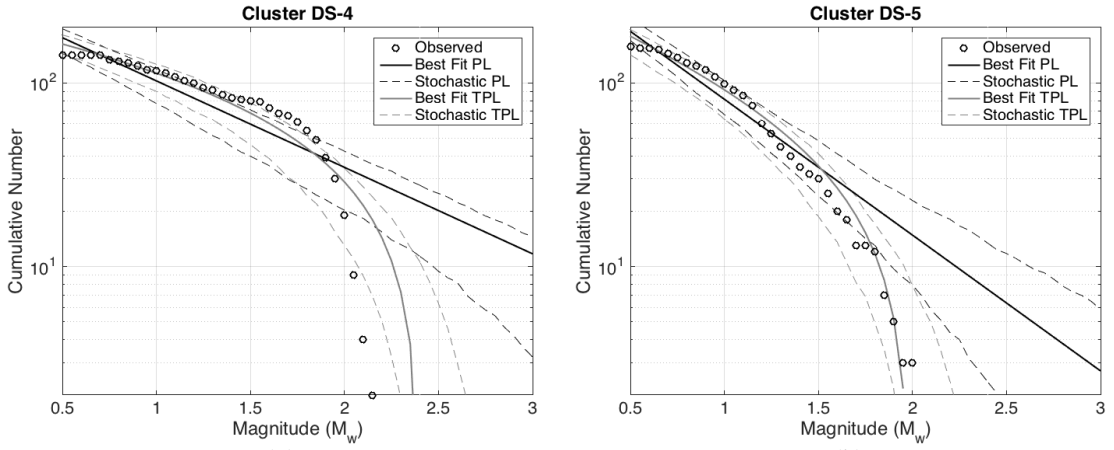

(a) *(b)*

Figure 11: Fitting PL (black) and TPL (grey) rupture area distributions to the DS-4 (a) and DS-5 (b) EMDs. Observed EMDs are shown by black circles. The solid lines show the best fitting models for a fixed $\Delta\sigma$ value, while the dashed lines show ± 2 standard deviations when $\Delta\sigma$ is varied stochastically.

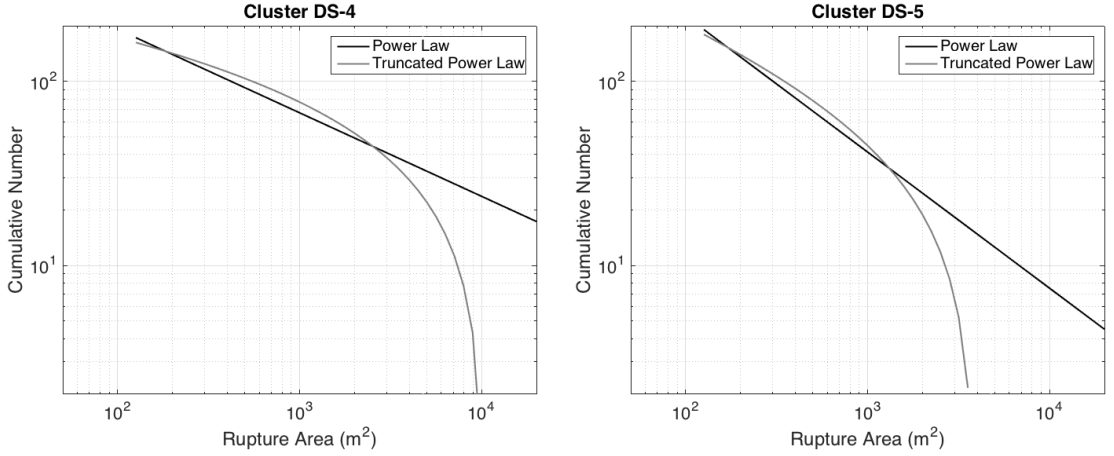

(a) *(b)*

Figure 12: Best fitting rupture area PL (black) and TPL (grey) distributions for the DS-4 (a) and DS-5 (b) clusters.

Based on these results, it is worth examining whether the best fitting values for A_{MAX} correspond to any length-scales associated with the mining activities. There are two length scales in play that might affect rupture dimensions: the width of the mining face (approximately 300 m); and the separations between (1) the underlying Parkgate Seam, which is 35 m below the Deep Soft (Figure 13), and (2) the overlying Top Hard Seam, which is approximately 110 m above the Deep Soft. Both seams have already been mined throughout our study area. The voids left by the longwall mining of these seams will be filled with goaf, the rubble and detritus created as the roof collapses behind the mining face. It is difficult to envisage a mechanism by which ruptures could propagate through such a rubble-filled void.

Assuming circular ruptures, areas of 10075 and 3870 m^2 correspond to rupture radii of 57 and 35 m. The larger dimension radius is therefore roughly equivalent to a circular rupture extending from the Deep Soft to the Top Hard. Alternatively, assuming a rectangular rupture, the DS-4 A_{MAX} value could correspond to a rupture with dimensions of approximately 35 × 300 m, equivalent to a rupture extending from the Deep Soft to the Parkgate, across the length of the mined face. In reality, ruptures will not be rectangular nor circular. Nevertheless, the general agreement between the dimensions of the maximum rupture area and these distances leads us to suggest that the presence of the overlying and underlying Top Hard and Parkgate seams is indeed limiting the rupture dimensions. Given the similarities between these dimensions, it is not possible to determine whether one of these features in particular is controlling the maximum rupture area. Indeed, it is likely that all three features: the width of the mining face; the distance to the underlying Parkgate Seam; and the distance to the overlying Top Hard Seam, are all playing a role in limiting the maximum rupture dimensions.

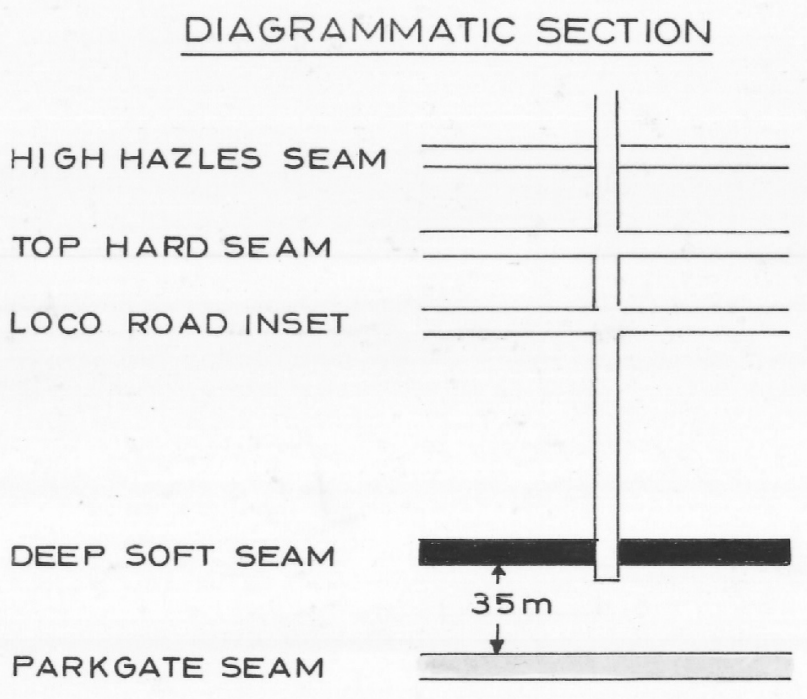

Figure 13: Diagrammatic section showing the spacing between the Deep Soft Seam, and the underlying Parkgate Seam, which has already been mined out across the study area. Image taken from UK Coal Authority Mine Abandonment Plans (2017).

5. Seismic Anisotropy and Shear-Wave Splitting

Shallow crustal anisotropy can be generated by several mechanisms, including: alignment of macroscopic fracture networks; the preferential alignment of microcracks due to anisotropic

stress field (in practice, the microscopic and macroscopic effects often combine, as both larger-scale fracture networks and microcracks are preferentially opened or closed by the same stress field); and by the alignment of sedimentary bedding planes.

Shear-wave splitting (SWS), where the velocity of a shear-wave is dependent upon the direction of travel and the polarity of the wave, is an unambiguous indicator of seismic anisotropy, and has been used previously to image stress changes induced by mining activities (Wuestefeld et al., 2011). Shear-waves that propagate near-vertically will not be sensitive to horizontally-layered sedimentary fabrics, which produce Vertically-Transverse-Isotropy (VTI) symmetry systems. Instead, in the absence of other major structural fabrics, the fast shear wave polarisation orientation can be treated as a proxy for the direction of maximum horizontal stress (e.g., Boness and Zoback 2006).

We perform SWS measurements on the Thoresby data. Accurate SWS measurements can only be obtained within the "S-wave window" (Crampin and Peacock 2008), because arrivals at an incidence angle greater than ~35° from vertical may be disturbed by S-to-P conversions at the free surface. This constraint limits the available data considerably, such that events within the S-wave window are found only on station NOLA, and for only 28 of the recorded events.

We perform the SWS measurement using the automated cluster-based approach described by Teanby et al. (2004). Where larger datasets are studied, automated quality assessments such as that described by Wuestefeld et al. (2010) can be used, but in this case, given the small sample size, the quality of measurements were assessed manually. Of the 28 arrivals within the S-wave window at NOLA, 9 provided good-quality, robust results according to the diagnostic criteria specified by Teanby et al. (2004). This is a typical rate-of-return for such studies given the relatively low magnitude (and therefore signal-to-noise) of the events. An example of a robust SWS measurement is provided in Figure 14

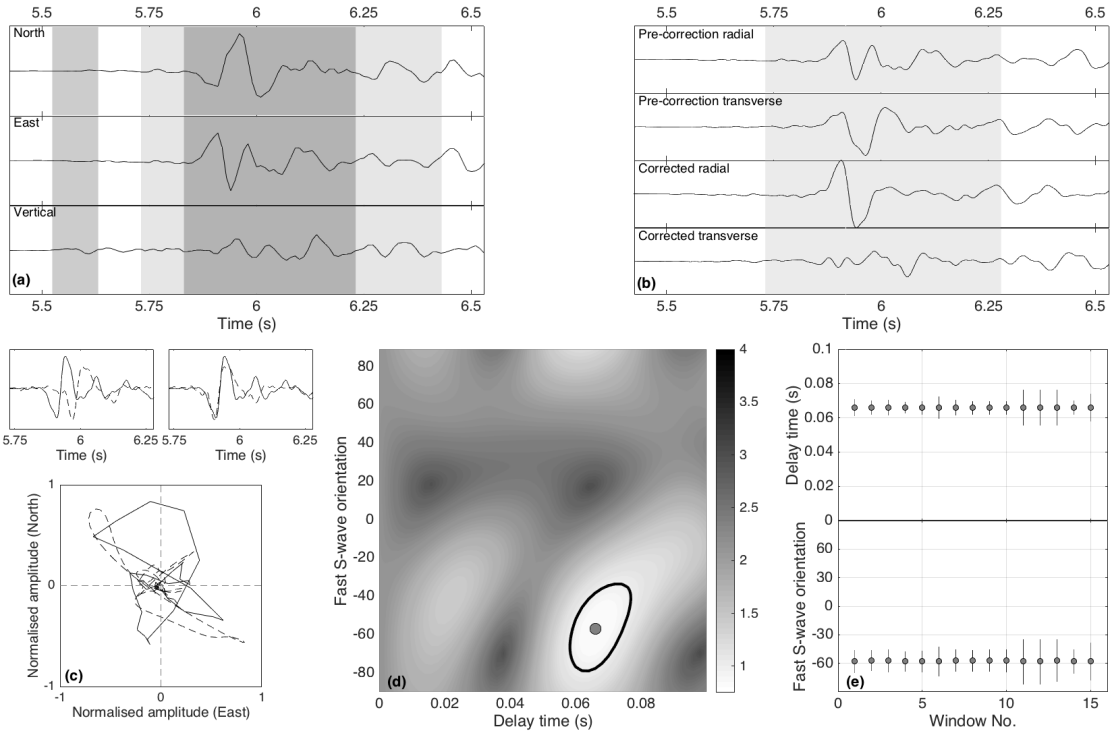

395

396 *Figure 14: Example shear-wave splitting measurement using the method described by Teanby et al.*
397 *(2004). In (a) we plot the N, E and Z components of the recorded waveforms, where P- and S-wave*
398 *windows are highlighted by the shaded areas. In (b) we plot the radial and transverse components*
399 *prior to and after the splitting correction, where the aim of the correction is to minimise energy on the*
400 *transverse component. In (c) we plot the waveform particle motions before (solid lines) and after*
401 *(dashed lines) correction. In (d) we plot the error surfaces of the correction method as a function of*
402 *delay time and fast direction normalised such that the 95% confidence interval (highlighted in bold) is*
403 *1. In (e) we plot the best-fit delay times and fast directions that result from choosing different S-wave*
404 *window start and end times (as indicated by the light-grey shaded zone of (a)).*

405 In Figure 15a we show the measured fast directions in the form of an angle histogram. A
406 dominant fast direction striking NW-SE is clearly observed. The mean fast direction azimuth
407 is 130°. No temporal variations in SWS fast directions or percentage anisotropy were
408 observed. The mean delay time was 43 ms, and the mean percentage S-wave anisotropy was
409 6.8%.

410 In Figure 15b we compare the measured fast S-wave orientations with independent
411 measurements for S_{Hmax} taken from the World Stress Map database (Heidbach et al., 2008).
412 These measurements, mainly from borehole breakouts and hydraulic fracturing tests, also
413 indicate an approximate regional S_{Hmax} strike that is to the NW-SE. We conclude that the
414 mean measured S-wave fast polarity of 130° can be used as a proxy for S_{Hmax} at this site.

415

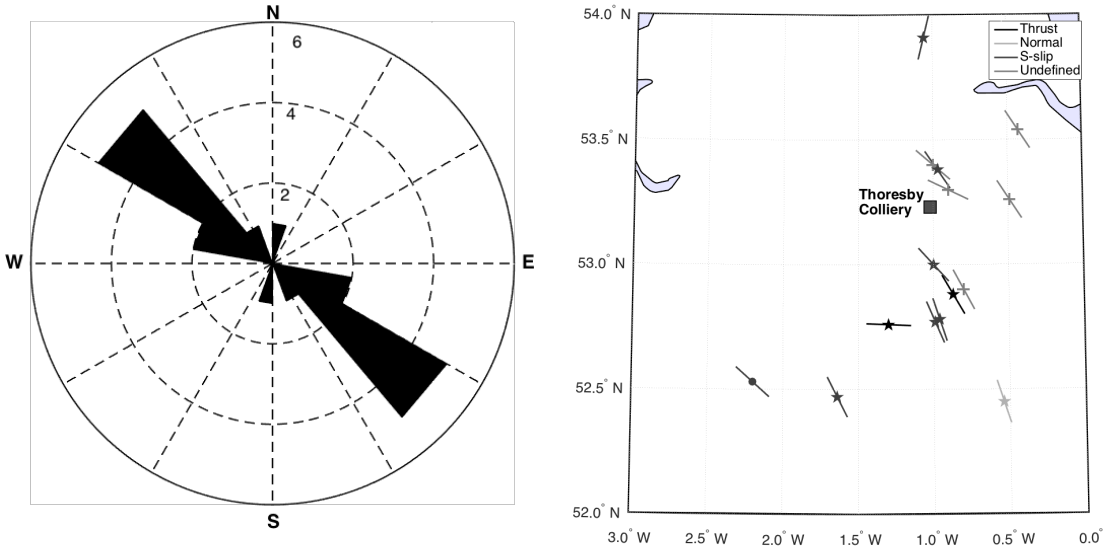

(a) *(b)*

Figure 15: SWS and stress anisotropy. In (a) we plot an angle histogram of the measured SWS fast directions. In (b) we show regional measurements of S_{Hmax} from the World Stress Map database (Heidbach et al., 2008): '+' symbols represent borehole breakouts, 'o' symbols represent focal mechanisms, and '★' symbols represent hydraulic fracturing data. The Thoresby site is marked by the red square. Measurements are coloure d by whether they represent a thrust, normal or strike-slip stress regime (if known).

6. Source Mechanisms

We compute event focal mechanisms by inverting the observed P-wave polarities and relative P-wave, S_H and S_V wave amplitudes for the best fitting double-couple source mechanism. In doing so, we preclude the possibility of non-double-couple sources in our inversion, as might be anticipated during mining-induced seismicity. We do this because the monitoring array consists of only 4 3-C and 3 1-C stations, which limits our ability to robustly constrain non-double-couple events. However, we note that the recovered mechanisms do a reasonable job of fitting the observed polarities, i.e. non-double-couple sources do not appear to be necessary to match the majority of our observations.

Of the 305 events, a total of 65 had sufficient signal-to-noise ratios such that P-wave polarities could be robustly assigned, and produced reliable and consistent source mechanisms. These strikes, dips and rakes for these events are plotted in Figure 16. We note 3 mains clusters of event types, representative source mechanisms for which are also plotted.

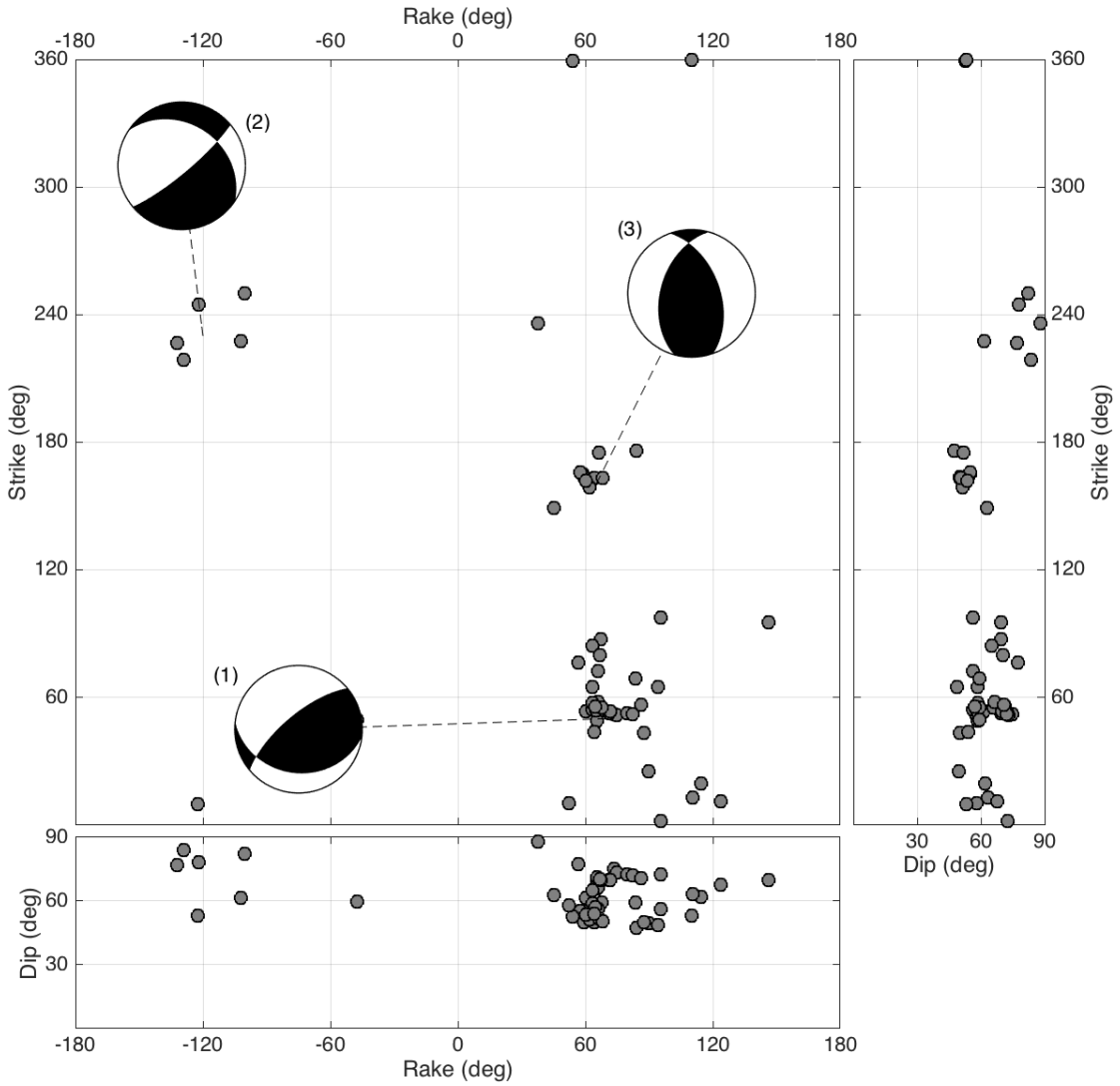

Figure 16: Source mechanisms (strike, dip and rake) for each event for which a reliable mechanism could be obtained. Three main clusters of mechanisms can be identified, representative focal spheres for which are shown. These spheres are upper-hemisphere projections where the compressive quadrants are shaded black.

The most common source mechanism type (numbered 1 in Figure 16) consists of events with strikes of approximately 50°, high angles of dip, and rakes of between 60° – 90°. This source mechanism orientation corresponds to near-vertical planes whose strikes match the strike of the mining face, on which dip-slip movement occurs, with the side of the fault that is towards the mine moving downwards.

A second, less populous source mechanism type (numbered 2 in Figure 16) shows similar strikes and dips, but with the opposite sense of movement such that the side of the fault towards the mining face moves upwards. Similar event mechanisms – near-vertical failure planes striking parallel to the mining face with upward and downward dip-slip motion – were observed by Bischoff et al. (2010) for longwall mines in the Ruhr Area, Germany, and we

share their geomechanical interpretation for these events (Figure 17). As the coal is mined, the surrounding rock mass will collapse to fill the void. This will result in downward motion of the overlying rock (as per source mechanism type 1), and upward motion of the underlying rock (as per source mechanism type 2) along vertical planes that run parallel to the mining face.

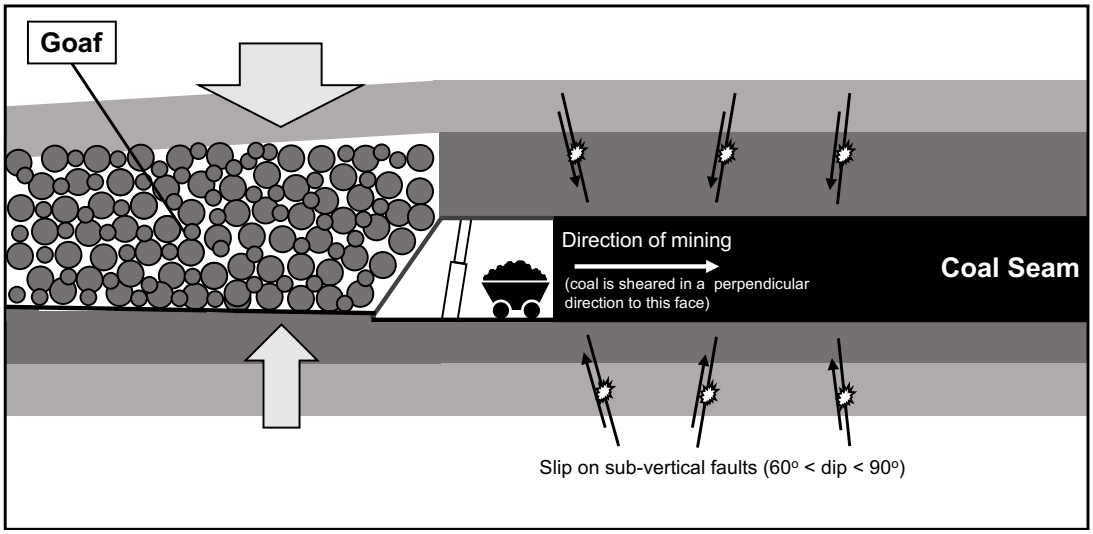

Figure 17: Geomechanical interpretation of the observed source mechanisms. As the surrounding rocks move to fill the void created by mining, dip-slip motion occurs on near-vertical slip planes oriented parallel to the mining face. Adapted from Bischoff et al. (2010).

A third type of source mechanism is also observed (numbered 3 in Figure 16), with thrust-type mechanisms occurring on steeply-dipping planes that strike approximately north-south. It is possible that they result from the interaction between mining activities and pre-existing structures in the area, since the N-S orientation of these planes does not match the orientation of any feature in the mine.

Using the source mechanisms for all events, we use the STRESSINVERSE iterative joint inversion algorithm described by Vavrycuk (2014) to estimate the orientations of principal stresses and the shape ratio, R (Gephart and Forsyth, 1984):

$$R = \frac{\sigma_1 - \sigma_2}{\sigma_1 - \sigma_3}, \quad (4)$$

where σ_1, σ_2, and σ_3 represent the maximum, intermediate and minimum principal stresses. The results of this inversion are listed in Table 3, and shown in Figure 18. We note that the resulting maximum horizontal stress is sub-horizontal, with an azimuth of 144°. This is consistent, within error, with the maximum horizontal stress orientation estimated from SWS analysis. This implies that, while the orientations of the slip planes are consistent with the geometry of the mining activities, the resulting deformation is also consistent with the regional *in situ* stress conditions.

Stress	*Azimuth*	*Plunge (down from horizontal)*	*Shape Ratio (R)*
σ_1	144°	31°	0.17
σ_2	52°	2°	
σ_3	319°	59°	

Table 3: Principal stress orientations and Shape Ratio (R) as inverted from event source mechanisms

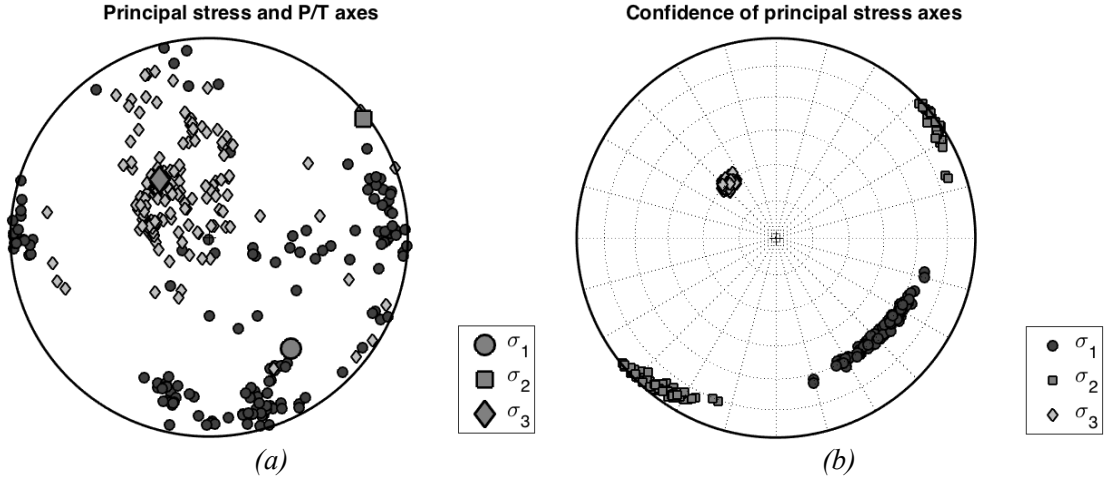

(a) *(b)*

Figure 18: Stress tensor inversion results using the STRESSINVERSE algorithm (Vavrycuk, 2014). In (a) we show a lower hemisphere projection of the P (dark grey ○) and T (light grey ◊) axes for every event, with the overall estimate for the σ_1, σ_2, and σ_3 axes marked by a large ○, □, and ◊, respectively. In (b) we show confidence limits for the principle stress axes, assuming ±15° error in source mechanism orientations.

6. CONCLUSIONS

In this paper, we characterise the seismicity recorded during longwall mining of the Deep Soft Seam at the Thoresby Colliery, Nottinghamshire, U.K.. A local monitoring network was installed for 8 months, recording 305 events, with the largest event having a local magnitude of M_L = 1.7. Event locations are found to track the advance of the mining faces, with most events being located up to 300 m ahead of the face.

We conclude that these events are “mining-induced”, i.e. they are directly induced by the mining activity, as opposed to “mining-tectonic” events, which are caused by static stress transfer producing activation of pre-existing tectonic faults. However, comparison between weekly mining rates and the rates of seismic activity do not show strong correlation. Moreover, the amount of deformation released in the form of seismic events is a small

494 percentage of the overall deformation produced by the mining activities (in other words, most
495 of the deformation is released aseismically).

496 Event magnitudes do not follow the expected Gutenberg-Richter distribution. Instead, we find
497 that the observed magnitude distribution can be reproduced by assuming that rupture areas
498 follow a Truncated Power Law distribution, whereby there is a limit to the maximum size of
499 the rupture area. The observed maximum rupture area could correspond to several controlling
500 features around the seam, including the width of the mining face, and the distances to the
501 underlying Parkgate and overlying Top Hard seams, which have already been excavated. Our
502 inference is that the presence of these rubble-filled voids where the excavated seams have
503 been mined out creates a limit to the maximum rupture dimensions.

504 Event source mechanism analysis shows that most events comprise dip-slip motion along
505 near-vertical planes that strike parallel to the orientation of the mining face. This type of
506 deformation is the expected response to the longwall mining process, and has been observed
507 at other longwall mining sites. The observed source mechanisms are also consistent with the
508 orientation of *in situ* regional stresses as inferred from SWS analysis.

509

510 **Acknowledgements**

511 JPV and JMK are funded by the BGS/University of Bristol Strategic Partnership in Applied
512 Geophysics. This work was performed as part of the Bristol University Microseismicity
513 Project (BUMPS).

514

515 **References**

516 Abercrombie R.E., 1995. Earthquake source scaling relationships from -1 to 5 M_L using
517 seismograms recorded at 2.5-km depth: Journal of Geophysical Research 100, 24015-
518 24036.
519 Allen R., 1982. Automatic phase pickers: Their present use and future prospects: Bulletin of
520 the Seismological Society of America 72, S225-S242.
521 Bischoff M., Cete A., Fritschen R., Meier T., 2010. Coal mining induced seismicity in the
522 Ruhr area, Germany: Pure and Applied Geophysics 167, 63-75.
523 Bishop I., Styles P., Allen M., 1993. Mining-induced seismicity in the Nottinghamshire
524 coalfield: Quarterly Journal of Engineering Geology 26, 253-279.
525 Boness N.L. and Zoback M. D., 2006. Mapping stress and structurally controlled crustal shear
526 velocity anisotropy in California: Geology 34, 825-828.
527 Bonnet E., Bour O., Odling N.E., Davy P., Main I., Cowie P., Berkowitz B., 2001. Scaling of
528 fracture systems in geological media: Reviews of Geophysics 39, 347-383.
529 Brune J.N., 1970. Tectonic stress and the spectra of seismic shear waves from earthquakes:
530 Journal of Geophysical Research 75, 4997-5009.

Burroughs S.M. and Tebbens S.F., 2001. Upper-truncated power laws in natural systems: Pure and Applied Geophysics 158, 741-757.

Burroughs S.M. and Tebbens S.F., 2002. The upper-truncated power law applied to earthquake cumulative frequency-magnitude distributions: evidence for a time independent scaling parameter: Bulletin of the Seismological Society of America 92, 2983-2993.

Butcher A., Luckett R., Verdon J.P., Kendall J-M., Baptie B., Wookey J., 2017. Local magnitude discrepancies for near-event receivers: Implications for the UK traffic light scheme: Bulletin of the Seismological Society of America 107, *in press*.

Cook N.G.W., 1976. Seismicity associated with mining: Engineering Geology 10, 99-122.

Crampin S. and Peacock S., 2008. A review of the current understanding of seismic shear-wave splitting in the Earth's crust and common fallacies in interpretation: Wave Motion 45, 675-722.

Edwards W.N., 1967. Geology of the country around Ollerton. Memoirs of the Geological Survey of Great Britain, Her Majesty's Stationery Office. Available online at: http://pubs.bgs.ac.uk/publications.html?pubID=B01568

Gephart J.W. and Forsyth D.W., 1984. An improved method for determining the regional stress tensor using earthquake focal mechanism data: Application to the San Fernando earthquake sequence: Journal of Geophysical Research 89, 9305-9320.

Gibowicz S.J., Harjes H-J., Schäfer M., 1990. Source parameters of seismic events at Heinrich Robert Mine, Ruhr Basin, Federal Republic of Germany: evidence for nondouble-couple events: Bulletin of the Seismological Society of America 80, 88-109.

Gutenberg B. and Richter C.F., 1944. Frequency of earthquakes in California: Bulletin of the Seismological Society of America 34, 185-188.

Hallo M., Oprsal I., Eisner L., Ali M.Y., 2014. Prediction of magnitude of the largest potentially induced seismic event: Journal of Seismology 18, 421-431.

Heidbach O., Tingay M., Barth,A., Reinecker J., Kurfeß D., Müller B., 2008. The World Stress Map Database Release 2008.

Hudyma M., Potvin Y., Allison D., 2008. Seismic monitoring of the Northparkes Lift 2 block cave – part 2 production caving: Journal of the Southern African Institute of Mining and Metallurgy 108, 421-430.

Kanamori H. and Brodsky E.E., 2004. The physics of earthquakes: Reports on Progress in Physics 67, 1429-1496.

Kwiatek G., Plenkers K., Dresen G., JAGUARS Research Group, 2011. Source parameters of picoseismicity recorded at Mponeng Deep Gold Mine, South Africa: Implications for scaling relations: Bulletin of the Seismological Society of America 101, 2592-2608.

Maxwell S.C., Shemeta J., Campbell E., Quirk D., 2008. Microseismic deformation rate monitoring: SPE Annual Technical Conference, Denver, SPE 116596.

McGarr A., 1976. Seismic moments and volume changes: Journal of Geophysical Research 81, 1487-1494.

McGarr A., 2014. Maximum magnitude earthquakes induced by fluid injection: Journal of Geophysical Research 119, 1008-1019.

Ottemöller L. and Sargeant S., 2013. A local magnitude scale M_L for the United Kingdom: Bulletin of the Seismological Society of America 103, 2884-2893.

Pacheco J.F., Scholz C.H., Sykes L.R., 1992. Changes in frequency-size relationship from small to large earthquakes: Nature 355, 71-73.

Podvin P. and Lecomte I., 1991. Finite difference computation of traveltimes in very contrasted velocity models: A massively parallel approach and its associated tools: Geophysical Journal International 105, 271-284.

580 Redmayne D.W., 1988. Mining induced seismicity in UK coalfields identified on the BGS
581 national seismograph network: in Bell F.G., Culshaw M.G., Cripps J.C., Lovell M.A.
582 (eds), *Engineering Geology of Underground Movements*, Geological Society Engineering
583 Geology Special Publication no. 5, 405-413.
584 Richter C.F., 1958. Elementary Seismology. Freeman and Co., San Francisco.
585 Sambridge M., 1999. Geophysical inversion with a neighbourhood algorithm –I. Searching a
586 parameter space: Geophysical Journal International 138, 479-494.
587 Sen A.T., Cesca S., Bischoff M., Meier T., Dahm T., 2013. Automated full moment tensor
588 inversion of coal mining-induced seismicity: Geophysical Journal International 195, 1267-
589 1281.
590 Scholz C.H. and Contreras J.C., 1998. Mechanics of continental rift architecture: Geology 26,
591 967-970.
592 Shapiro S.A., Krüger O.S., Dinske C., 2013. Probability of inducing given-magnitude
593 earthquakes by perturbing finite volumes of rocks: Journal of Geophysical Research 118,
594 3557-3575.
595 Stec K., 2007. Characteristics of seismic activity of the Upper Silesian Coal Basin in Poland:
596 Geophysical Journal International 168, 757-768.
597 Stork A.L., Verdon J.P., Kendall J-M., 2014. The robustness of seismic moment and
598 magnitudes estimated using spectral analysis: Geophysical Prospecting 62, 862-878.
599 Teanby N.A., Kendall J-M., van der Baan M., 2004. Automation of shear-wave splitting
600 measurements using cluster analysis: Bulletin of the Seismological Society of America 94,
601 453-463.
602 Turvill W., 2014. Welcome to Britain's earthquake capital: Sleepy Nottinghamshire town has
603 been hit by 36 tremoers in just 50 days – and geologists say mining is to blame: The Daily
604 Mail, accessed from http://www.dailymail.co.uk/news/article-2548146/Welcome-Britains-
605 EARTHQUAKE-capital-Sleepy-Nottinghamshire-town-hit-36-tremors-just-50-days-
606 geologists-say-mining-blame.html on 21.01.2017.
607 UK Coal Authority Mine Abandonment Plans, 2017. Mine Abandonment Plans are available
608 upon application to the UK Coal Authority. See https://www.gov.uk/guidance/coal-
609 mining-records-data-deeds-and-documents
610 Vavrycuk, V., 2014. Iterative joint inversion for stress and fault orientations from focal
611 mechanisms: Geophysical Journal International 199, 69-77.
612 Wesnousky S.G., Scholz C.H., Shimazaki K., Matsuda T., 1983. Earthquake frequency
613 distribution and the mechanics of faulting: Journal of Geophysical Research 88, 9331-
614 9340.
615 Wilson M.P., Davies R.J., Foulger G.R., Julian B.R., Styles P., Gluyas J.G., Almond S., 2015.
616 Athropogenic earthquakes in the UK: a national baseline prior to shale exploitation:
617 Marine and Petroleum Geology 68, 1-17.
618 Wuestefeld A., Al-Harrasi O., Verdon J.P., Wookey J., Kendall J-M., 2010. A strategy for
619 automated analysis of passive microseismic data to image seismic anisotropy and fracture
620 characteristics: Geophysical Prospecting 58, 755-773.
621 Wuestefeld A., Kendall J-M., Verdon J.P., van As A., 2011. *In situ* monitoring of rock
622 fracturing using shear wave splitting analysis: an example from a mining setting:
623 Geophysical Journal International 187, 848-860.
624 Younger P.L., 2016. How can we be sure fracking will not pollute aquifers? Lessons from a
625 major longwall coal mining analogue (Selby, Yorkshire, UK): Earth and Environmental
626 Science Transactions of the Royal Society of Edinburgh 106, 89-113.
627
628